

HONORS CAPSTONE MAY 5, 2023

**Probing the Properties of Interstellar Dust
Towards the Hot Star Zeta Ophiuchi**

BROCK A. PARKER ¹ AND HENRY A. KOBULNICKY ¹

¹*Department of Physics & Astronomy, University of Wyoming, Laramie, WY 82070, USA*

Corresponding author: Brock A. Parker
bparke13@uwyo.edu, brockaustin09@gmail.com

ABSTRACT

Microscopic dust grains permeate the interstellar medium, blocking and obscuring light from all sources. This effect is termed interstellar extinction. Varying amounts and sizes of dust cause different amounts of extinction at different wavelengths of light which can be probed through the total amount of extinction, A_V , an indicator for the amount of dust, and R_V , an indicator for the size of the dust. In order to characterize the dust and construct the reddening curves in a known dusty region, we obtained *Hubble Space Telescope* Space Telescope Imaging Spectrograph ultraviolet spectra for five bright stars lying behind the highly irradiating hot star ζ Ophiuchi. Combining these spectra with archival photometric data, the extinction curves for each star in the sample are constructed and the best fit parameters calculated. Best fit models show interstellar average $R_V \approx 3.0$ for ζ Ophiuchi and a significantly lower $R_V \approx 2.3$ for the target stars, indicating non-standard small dust grains. Such small dust grains are likely due to high levels of irradiation, systematically lowering the average dust grain size.

Keywords: Ultraviolet astronomy(1736)

1. INTRODUCTION

As light from astrophysical sources travels through space to Earth, it must first pass through the interstellar medium (ISM), the combination of dust and gas that permeates the space in between stars. Much like fog on a cold summer morning, this dust attenuates and reddens the light passing through it. As such, it is imperative to understand the effects of such dust in order to correct for it, as well as the varying effects that different extreme environments have on the properties of this dust. We investigate the properties of the dust clouds towards ζ Ophiuchi, a hot highly irradiating star above the disk of the Milky Way. It is suspected the extreme irradiation systematically reduces the dust grain population sizes (Draine 2011; Maíz Apellániz, J. & Barbá, R. H. 2018). We characterize this dust both to inform observational corrections along the line of sight and to draw a connection between irradiation and dust grain demographics.

1.1. Evidence for Interstellar Material

The first evidence of interstellar dust was the blocking and dimming, or extinction, of star light along selective lines of sight (Barnard 1910). Such shadows are visible in the vast dust lanes obscuring the light from the center of the Milky Way galaxy, as seen in Figure 1. Such observations, as well as more detailed studies of individual stars, lead to the realization that there is material lying in the path of the incoming starlight, first theorized to be “fine cosmic dust particles of various sizes” (Trumpler 1930). More detailed analysis of the specifics of this dimming from interstellar dust,



Figure 1. Prominent dust lanes toward the center of the Milky Way. This dust blocks the light from background stars, casting a visible shadow onto Earth-based observers.

referred to as extinction or attenuation, reveals further details about the composition and makeup of this dust.

Historically, calculating the amount of extinction present for a given source source involved comparing the light from a star with known extinction to that of a star with no extinction. This method, the pair method, allows for rough approximations of how the extinction changes with the wavelength of light, and is still one of the main methods to study dust today, with slight modifications.

Several other observations have since followed that further support interstellar dust. Some of which include: wavelength dependent polarization of starlight, scattered light in reflection nebulae, sub-millimeter thermal dust emission, scattered x-ray halos, extended red microwave emission, interstellar elemental depletion, and still others (Draine 2011). While not discussed here, each of these observational effects constrain the amount, sizes, and compositions of interstellar dust.

With the rise of spectroscopy also came the rise of spectroscopic extinction curves, resulting in high-fidelity measurements of the wavelength dependence of extinction. Additionally, as both computer-generated spectra become increasingly precise, these dependencies are calculated with significantly smaller systematic errors, still echoing the same methods from before.

1.2. *Effects of Interstellar Dust*

Dust both scatters and absorbs light passing through it, stealing valuable photons from the sources behind. The total amount of extinction at a given wavelength, A_V , is defined as the difference in magnitudes between the intrinsic (unobscured) flux F_λ^0

and the observed flux F_λ . This quantity is thus a probe for the total amount of dust between the source and observer,

$$A_\lambda = 2.5 \log \left(\frac{F_\lambda^0}{F_\lambda} \right). \quad (1)$$

Plotting extinction versus wavelengths—the extinction curve—reveals that extinction depends strongly on wavelength. Specifically, there is more extinction at shorter blue wavelengths than at longer red wavelengths. As such, observed extinguished spectra will appear redder than the intrinsic spectra, an effect hereafter referred to as simply ‘reddening.’

The amount of reddening, $E(B - V)$, is the difference in magnitude between the B band and V band, $E(B - V) = A_B - A_V$ (Cardelli et al. 1989; Draine 2011). The slope of the extinction curve in the optical regime, R_V , is defined as the ratio of visual extinction A_V to reddening $E(B - V)$. Cardelli et al. (1989) showed this quantity can be used in combination with A_V to fully parameterize extinction curves. Additionally, R_V has been shown to have a correlation with the size of the interstellar dust grains along the line of sight, thereby defining the shape of the extinction curve (Kim & Martin 1996).

$$R_V = \frac{A_V}{E(B - V)} \quad (2)$$

Figure 2 illustrates both reddening and total extinction. The x-axis is the rest frame wavelength in Angstroms, and the y-axis is the flux density, brightness, at a given wavelength. The black curve shows the intrinsic, unobstructed, spectrum from a hot star. Much of the flux from the star originates in the ultraviolet and visible region. The red curve shows the same spectrum extinguished by an average dust cloud. Not only is the entire spectrum dimmed, the ultraviolet wavelengths, towards the left, are extinguished notably more than infrared wavelengths, toward the right, shifting the entire shape of the spectrum. If the presence of the dust cloud was unknown, observers may draw incorrect conclusions about the source of the spectrum.

This wavelength dependence of dust extinction arises from Mie scattering theory, which governs the interactions between electromagnetic waves and particulates. Mie theory postulates that there is a strong relationship between the ratio of the incident light wavelength to grain size with the efficiency of scattering (Mie 1908). We thus expect a non-constant relationship between extinction and wavelength; moreover, it follows as well that different sizes of dust grains are expected to produce wavelength dependent extinction curves, as seen in Kim & Martin (1996).

1.3. *Composition of Interstellar Dust*

The aforementioned observed properties and effects of dust work to constrain the composition of interstellar dust grains. From the large wavelength range of extinction from the UV to infrared, dust grains must similarly span a very large range

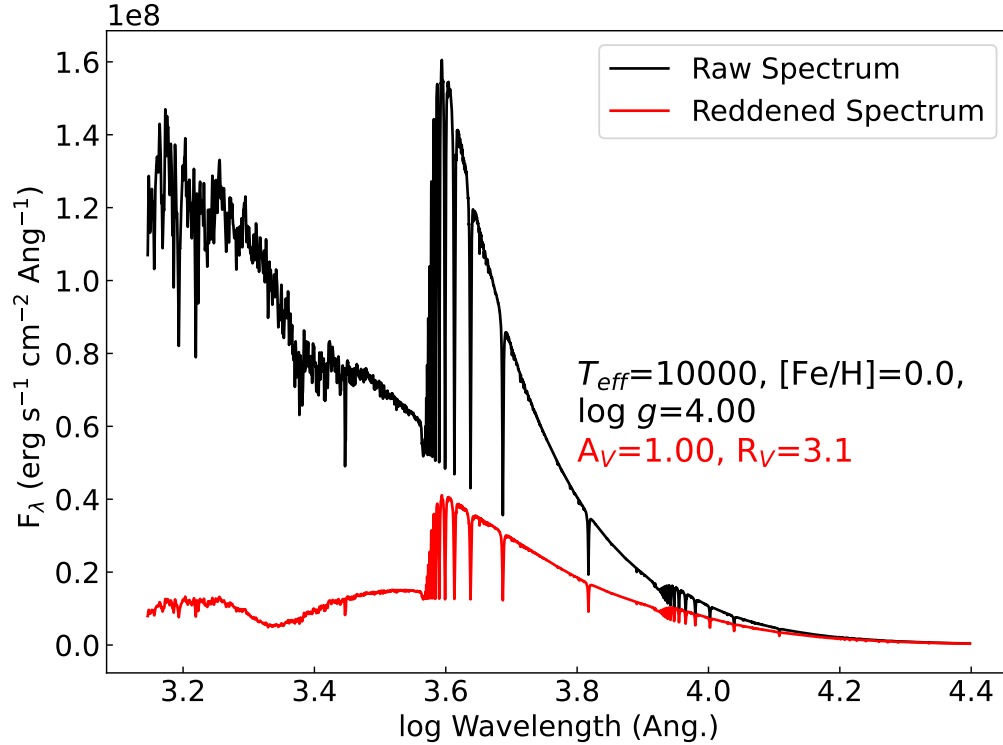


Figure 2. Intrinsic stellar spectrum (black) compared to the observed reddened spectrum (red). Bluer wavelengths are extinguished more than red wavelengths, resulting in the overall ‘reddening’ of the spectrum.

of sizes, from radii of approximately $0.01 \mu\text{m}$ to around $1 \mu\text{m}$. Physical scattering laws motivate these limits, as large dust grains would produce perfectly gray scattering, whereas small dust grains would produce Rayleigh scattering with very steep extinction curves (Draine 2011).

While the size of dust grains spans this range, the size distribution of dust grains is not constant. By constructing theoretical extinction curves from scattering laws and dust grain models, Mathis et al. (1977) found a nearly power-law distribution of grain sizes across the entire size domain with more small dust grains than large. They found such distributions consistently no matter the grain material. Modern extinction curves (e.g., Weingartner & Draine 2001) still echo these power law distributions, pointing towards stochastic dust formation scenarios.

In order to replicate the shape of the observed extinction curves—specifically the large ‘bump’ around 2175 \AA (see Stecher & Donn 1965), Mathis et al. (1977) explored a combination of different suspected interstellar materials, such as graphite, enstatite, olivine, silicon carbide, and magnetite. Throughout all different models, they found that all combinations required graphite to reproduce the observed bump plus an additional material to reproduce the rest of the extinction curve.

Other specific extinction curve features shed insight on the composition of the interstellar dust. Some of these features include the 2175 \AA bump, silicate features

at $9.7 \mu\text{m}$ and $18 \mu\text{m}$, $3.4 \mu\text{m}$ bump, and diffuse interstellar bands (Draine 2011). Combining the strengths and locations of these broad spectroscopic features with line of sight abundances from dusty regions with bright stars, it has been possible to limit the materials comprising interstellar dust to silicates, carbonaceous materials, carbonates, hydrocarbons, and silicon carbide (Draine 2011; Mathis et al. 1977).

While the existence of the 2175 \AA bump, along with other absorption features, are almost certainly due to specific carbon bond transitions, where this carbon is stored in the chemical structure of the interstellar dust is still unknown. Many modern models attribute these features to polycyclic aromatic hydrocarbons (PAHs), organic compounds composed of multiple aromatic rings. The inclusion of these molecules results in size distributions that no longer follow a power law (Weingartner & Draine 2001).

Figure 3 illustrates a modern interstellar dust grain size distribution from Weingartner & Draine (2001). The x-axis is grain size, and the y-axis is the number density scaled by a^4 to flatten out the curve. The original size distribution as defined by Mathis et al. (1977) is shown as a heavy line. The top plot shows the distribution for silicates, and the bottom shows the distribution for carbonaceous materials, including PAHs. While both curves still roughly follow a power-law (see Mathis et al. 1977), the carbonaceous materials require additional peaks and valleys to properly explain observed extinction curves. Additionally, Weingartner & Draine (2001) showed that the grain size distributions, as calculated from extinction curves, have a strong correlation with R_V .

One important caveat to the extinction curve morphology discussed hitherto is the assumption of average dust. All presented extinction curves and size distributions model average dust along lines of sight in the Milky Way Galaxy. There are many known extreme lines of sight that deviate far from these average extinction curves, such as the Large (LMC) and Small Magellanic Clouds (SMC) (Gordon et al. 2003). The abnormal shape of these extinction curves provide clues to the formation and evolution of the dust grains in these extreme environments. Figure 4 shows the atypical extinction curves for the LMC and SMC compared with the average Milky Way extinction curve. As before, the x-axis is inverse wavelength in μm and the y-axis is amount of extinction in magnitudes. The Milky Way average, the dot-dashed line, shows a much stronger bump and shallower far-UV rise than the LMC and SMC extinction curves. For the bar of the SMC, the solid line, there is almost no bump present with a relatively steep far-UV rise, indicating a different dust grain composition in these galaxies.

1.4. Reddening Laws

The extinction curves presented so far have been derived empirically from measured extinction of various objects along different lines of sight (Johnson 1965; Cardelli et al. 1989; Fitzpatrick et al. 2019). It is thus of great interest to derive models in order to

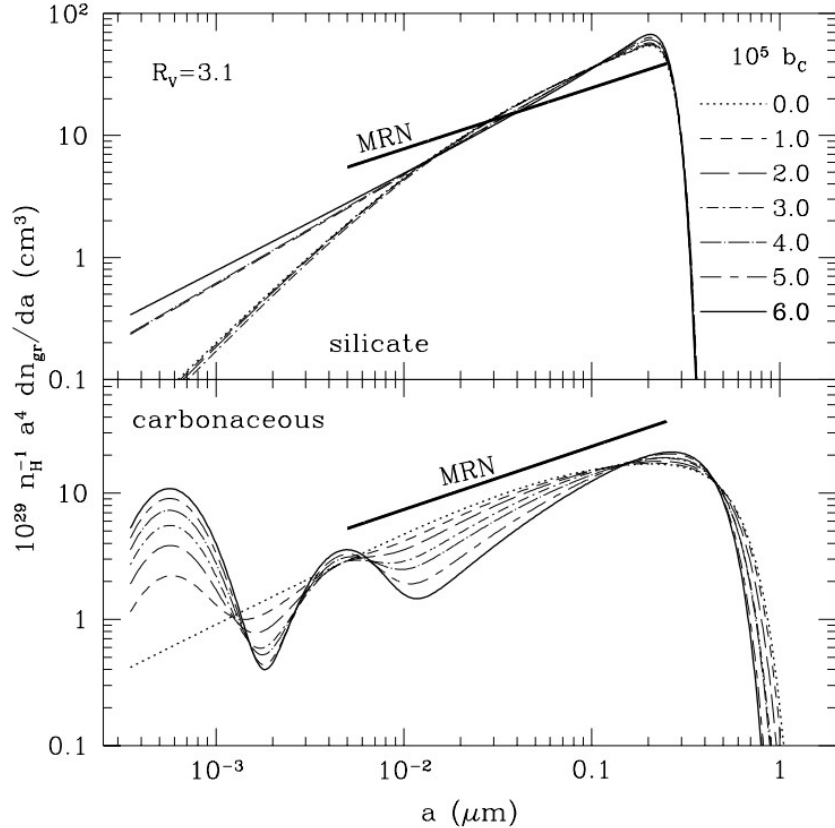


Figure 3. Dust grain size distribution for average Milky Way dust assuming a combination of silicates and carbonaceous materials, including PAHs. *Top:* The calculated sizes for silicates. *Bottom:* The calculated size distribution for carbonaceous materials. The silicates follow a classical power-law, while the carbon-carrying materials have dips and valleys laid on top of a power-law. Both curves rapidly drop off for very large dust grains where formation of particles that large is very unlikely and difficult to achieve (Weingartner & Draine 2001).

make predictions for extinction along sight lines with unknown dust and reddening. Fitzpatrick & Massa (1988) derived a fit using a physically motivated model consisting of six independent parameters to fully describe the shape of the extinction curve from the optical to the far-UV. These six parameters are then empirically derived for each line of sight using measured extinction curves, allowing for the dereddening of spectra along that given line of sight. However, these curves still require prior knowledge of the reddening for each sightline, making it less ideal for dereddening arbitrary dust.

The desire for simple yet comprehensive predictive dust models culminated in many of the extinction curves present today. Many dust studies have come to the conclusion that much of the dust in the Milky Way follows the same shape of extinction curve, simply shifted up or down depending on the amount of dust. Using the six derived parameters from Fitzpatrick & Massa (1988), Cardelli et al. (1989) parameterized the curves using both A_V and R_V as predictors for those six parameters. A_V determines the vertical shift of the extinction curve and R_V determines the overall shape, with $R_V = 3.1$ taken to be the approximate average for the Milky Way (Savage & Mathis

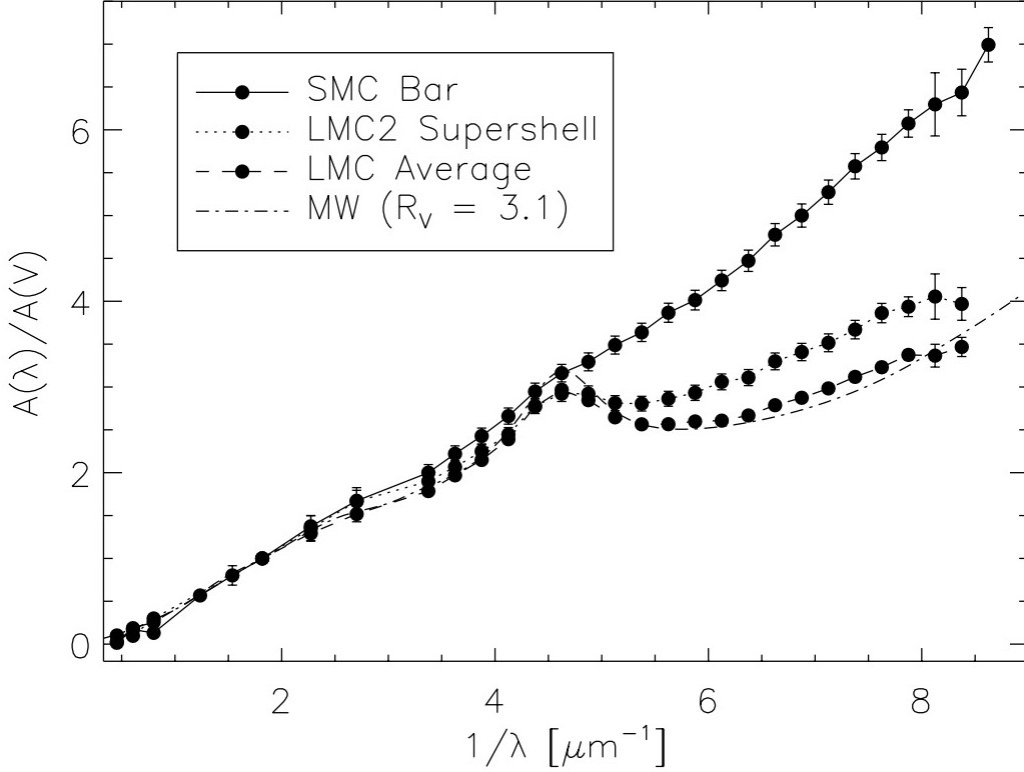


Figure 4. Extinction curves for the bar of the Small Magellanic Cloud (solid line), the Large Magellanic Cloud average (dashed line), a sub-region of the Large Magellanic Cloud (dotted line) and the Milky Way average (dashed-dotted line). The Magellanic clouds, especially the SMC, have noticeably weaker 2175 Å bumps as well as different far-UV rises (Gordon et al. 2003).

1979; Cardelli et al. 1989; Draine 2011). Thus, by assuming the dust has the same composition as the Milky Way, extinction curves can be predicted along arbitrary sight lines, and these predictions are a proxy for both the size of the dust and the total amount of dust (Draine 2011). However, such models are only valid for Milky Way average dust.

Many other Milky Way average R_V dependent extinction curve models have been constructed (see Cardelli et al. 1989; Fitzpatrick et al. 2019; Gordon et al. 2023). Most of these modern curves are updates of the original Cardelli et al. (1989) curve with modern data and fitting techniques. Additionally, some curves extend into further wavelength ranges, using data from IR and far-UV telescopes. We employ three of these reddening laws, including Cardelli et al. (1989), to deredden our spectra. Figure 5 shows a comparison of different extinction curve models for different R_V s. All model curves have $A_V = 1$. The x-axis is inverse wavelength in μm and the y-axis is amount of extinction in magnitudes. The different style curves show different models for average Milky-Way dust extinction curves. Different color curves show different reddening. As the reddening increases, the slope of extinction curves decrease, resulting in less overall extinction across the entire spectrum. For all the curves, the

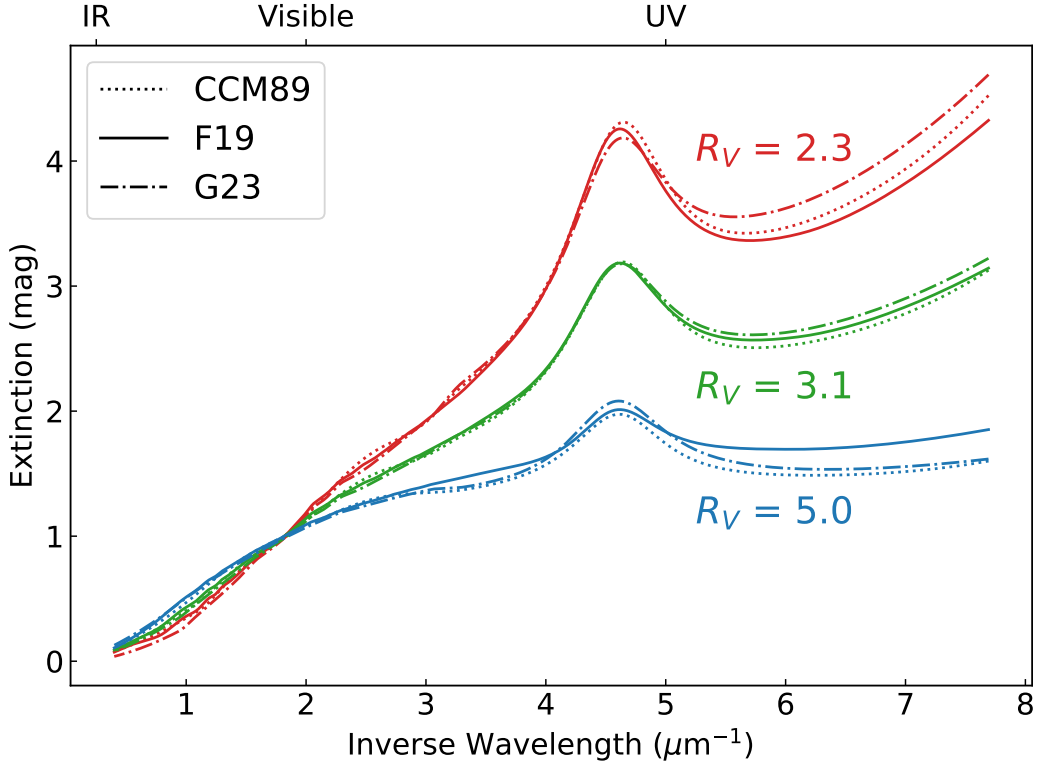


Figure 5. Comparison of different extinction curve models. Each model has the same $A_V = 1$ and the three different models (Cardelli et al. (1989); Fitzpatrick et al. (2019); Gordon et al. (2023)) are each shown for three different R_V values spanning the range of known extreme dust.

total amount of extinction increases as the wavelength decreases. Additionally, there is a large bump near $5 \mu m^{-1}$ —the 2175 \AA bump—thought to be caused by specific dust grains. For all of these laws, the differences in extinction are most visible in the ultraviolet and infrared, making hot stars ideal probes of different dust grain sizes.

From these curves, the effects of different dust grain size distributions as probed by R_V are immediately visible; smaller dust produce more extinction in the ultraviolet relative to longer wavelengths, whereas larger dust grains produce less extinction in the ultraviolet relative to longer wavelengths. Analytically, such behavior makes sense, as arbitrarily large dust grains would produce completely flat extinction, so called ‘grey’ dust, whereas small dust grains would produce Rayleigh scattering, which shows a much steeper slope than any of the reddening laws predict.

It is again important to note that these analytical reddening laws are only valid for average Milky Way dust. In atypical regions, such as the LMC and SMC, these laws are insufficient to model and predict the extinction curves seen. As well, even within the Milky Way, many anomalous sightlines are known, some which lack bumps, some that have a step far-UV rise, and some that show enhanced bump features (Gordon et al. 2003). More complicated models, such as physical dust grain models (see Weingartner & Draine 2001), are needed to accurately characterize the dust along

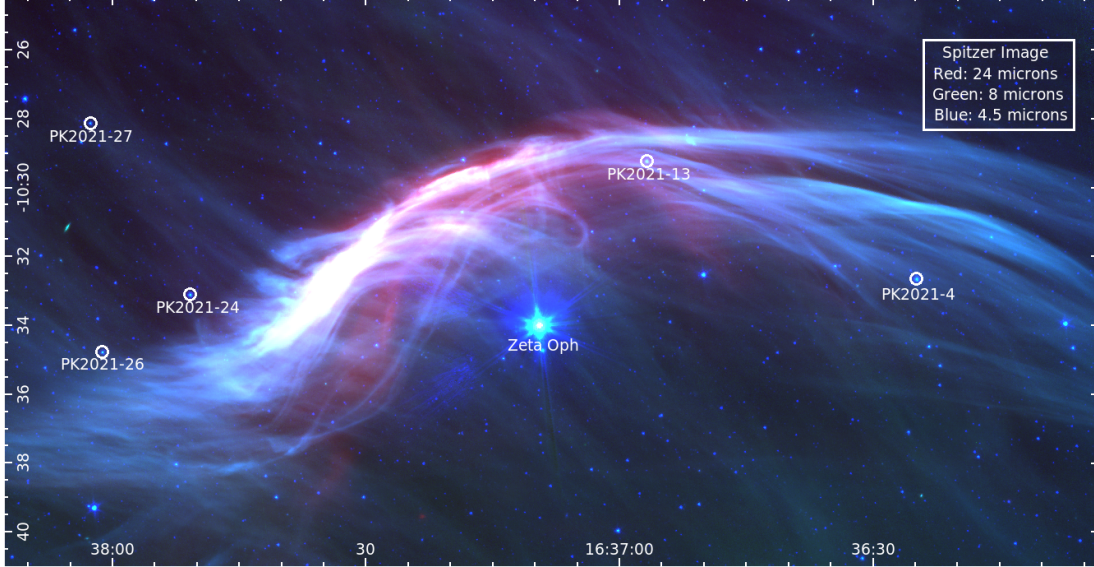


Figure 6. The field surrounding ζ Ophiuchi as seen from *Spitzer* images. The bowshock nebula preceding ζ Oph can be seen clearly in red ($24 \mu\text{m}$). Faint dust striations can be seen in green ($8 \mu\text{m}$) that run across the entire field.

these lines of sight. However, these basic models are useful for flagging such extreme extinction curves for additional follow up.

2. OBSERVATIONS AND DATA

2.1. ζ Ophiuchi Sightline

In order to investigate the characteristics of extreme interstellar dust, we examine stars along the sightline toward ζ Ophiuchi, a hot O9.2IV star lying above the galactic plane. The dusty region immediately surrounding ζ Oph is diffuse and highly irradiated, making it an ideal testing ground for the properties of extreme dust. Moreover, ζ Oph lies nearby, with a Gaia estimate of 182^{+53}_{-34} pc, with a well studied foreground consisting of normal Milky Way dust (Cardelli et al. 1989; Morton 1975). This allows for accurate and precise measurements of dust properties along the sightline, including a unique opportunity for dust property breakdown by distance (see Piccone & Kobulnicky 2022).

Figure 6 shows the region surrounding ζ Ophiuchi as seen in the infrared from the *Spitzer Space Telescope*. Red represents $24 \mu\text{m}$, green $8 \mu\text{m}$, and blue $4.5 \mu\text{m}$. Immediately preceding ζ Oph is a bright bow shock nebula extending across a large angular space. Additionally, faint striated dust filaments run across the image, approximately aligned with the motion of ζ Oph. The large angular size of these features spans various stars, creating a great laboratory for investigating the dust features across all dimensions of the dust clouds.

2.2. UV Spectra and Photometry

We selected five of the brightest stars in the ultraviolet immediately surrounding ζ Ophiuchi based on the sample identified in Piccone & Kobulnicky (2022). From

Table 1. Gaia Stellar Parameters for Selected Targets in ζ Ophiuchi Field

Target	Gaia ID	R.A. (deg.)	Decl. (deg.)	T_{eff} (K)	$\log g$	d (pc)	[M/H]
PK-04	4338102923864645120	249.1036	-10.5442	5722^{+16}_{-32}	$4.127^{+0.0024}_{-0.0037}$	223^{+9}_{-5}	$-0.218^{+0.010}_{-0.022}$
PK-13	4338104126455487488	249.2367	-10.4871	6634^{+6}_{-13}	$3.945^{+0.0011}_{-0.0026}$	449^{+20}_{-8}	$-0.231^{+0.004}_{-0.004}$
PK-24	4337372852442084096	249.4617	-10.5519	5091^{+92}_{-221}	$4.307^{+0.0010}_{-0.0037}$	202^{+6}_{-21}	$-0.800^{+0.104}_{-0.470}$
PK-26	4337371787290173952	249.5049	-10.5797	6731^{+16}_{-34}	$3.898^{+0.0022}_{-0.0021}$	669^{+18}_{-19}	$-0.473^{+0.012}_{-0.014}$
PK-27	4337375218965869568	249.5108	-10.4688	6672^{+19}_{-74}	$4.134^{+0.0007}_{-0.0012}$	499^{+6}_{-5}	$-0.608^{+0.017}_{-0.051}$

this sample, we obtained *Hubble Space Telescope* (*HST*) STIS G230L spectra from 1600 to 3100 Å for targets PK-04, PK-13, PK-24, PK-26, and PK-27. The resulting data was reduced using the typical *HST* pipeline. Table 1 gives the *Gaia* stellar parameters for the target stars. Column one lists the target name. Column two is the *Gaia* DR3 ID. Columns four and five are the right ascension and declination, respectively. Columns six, seven, and eight give the best estimates of surface gravity, parallactic distance, and metallicity, respectively, as determined from *Gaia* DR3 photometric measurements. Due to the incredibly high flux from ζ Ophiuchi across all wavelengths, precision *HST* spectra could not be obtained. Rather, archival *International Ultraviolet Explorer* (*IUE*) spectra were obtained spanning nearly the same wavelength range as the *HST* observations.

Figure 9 shows the observed *HST* spectra for each star. The x-axis is wavelength in Å and the y-axis is flux density in $\text{erg s}^{-1} \text{cm}^{-2} \text{Å}^{-1}$. While some of the stars have measurable flux in the far-UV range, most of the targets do not contain enough flux at these short wavelengths to properly constrain the far-UV rise of the extinction curve; however, all of the targets have sufficient flux and precision to measure the strength of the 2175 Å bump as well as differentiate different R_V values.

In order to more precisely constrain the reddening parameters for the selected target stars, we also retrieved archival AAVSO Photometric All-Sky Survey (APASS) DR9 photometry for all of the target stars, including ζ Oph, in B, V, g, r, i, z, J, H, K, W1, and W2 bandpasses (Henden et al. 2016). These magnitudes were then converted into absolute fluxes using the Space Telescope Science Institute (STScI) WFC3 flux conversion tool as defined in Bohlin et al. (2020). All photometric observations were taken to have a standard error of five percent.

Since around half of all stars are in binary or higher systems, (see Duchêne & Kraus 2013) it is important to take this into account when modelling the spectrum of stars extinguished by dust. In order to investigate the probability of contamination from potential binary sources, we looked at both *Gaia* Renormalized Unit Weight

Table 2. Gaia Multiplicity Indicators for Targets from Table 1

Target	V_r (km/s)	RUWE	Δv (km/s)
PK-04	-28.09 ± 0.28	1.447	5.68 ± 6.16
PK-13	29.31 ± 0.46	1.031	12.32 ± 9.81
PK-24	-41.18 ± 0.45	1.140	5.08 ± 8.68
PK-26	-0.62 ± 1.88	2.446	8.01 ± 16.46
PK-27	17.98 ± 0.73	0.947	-

Error (RUWE) and velocity dispersion. RUWE is a description of how well the calculated spectroscopic model fits the photometric data from *Gaia* (Lindegren et al. 2018). For single stars this number should be around 1.0, and anything less than 1.4 is considered an indicator of a good astrometric solution. Similarly, any value over 2.0 is considered poor and indicates a very poor fit to the data due to either poor parameters or stellar multiplicity. Additionally, the error in the velocity dispersion of each target is an indicator of multiplicity; binary stellar spectral features will appear broadened. Table 2 gives these values for our targets. The first column is the target name, the second gives the radial velocity, the third column gives the RUWE, and the fourth gives the velocity dispersion. For targets 4, 13, 24, and 27, we find little evidence to suggest binary systems. However, for PK2021-26, there is strong evidence for multiplicity from both the large RUWE and error on the velocity dispersion.

3. ANALYSIS

In order to equally weight both the spectral and photometric data, we binned the UV spectra for each target star into 10 bins to match the number of photometric data points available. We spaced the bins evenly along the entire wavelength range of the measured spectra, regardless of low signal-to-noise ratio at very short wavelengths. After binning, we took an average approximate error for each bin of five percent, motivated by the physical error reported in the measured spectra.

In order to derive the reddening parameters for each target star, we constructed the intrinsic spectrum of each star using PHOENIX stellar models (Husser et al. 2013). The metallicity and surface gravity for each star were taken to be the best reported values from *Gaia* DR3. Due to the large degeneracy between metallicity and reported reddening, metallicity values were interpolated between provided models for a given surface gravity and temperature. The temperature for each star was taken as the nearest provided model to the temperatures derived in Piccone & Kobulnicky (2022), which are in good agreement with the temperatures used as radial velocity templates for *Gaia* DR3.

Table 3. Best fit reddening parameters for target stars

Target	F19			CCM89			G23		
	A_V	R_V	χ^2	A_V	R_V	χ^2	A_V	R_V	χ^2
PK-04	0.876	2.115	6.814	0.855	2.084	6.436	0.940	2.300	6.305
PK-13	1.313	2.352	3.926	1.286	2.356	3.018	1.231	2.362	2.249
PK-24	0.882	2.000	4.249	0.631	1.465	1.990	0.968	2.300	6.637
PK-26	1.123	2.389	2.933	1.105	2.374	2.607	1.058	2.361	2.014
PK-27	0.909	2.381	5.048	0.874	2.318	4.631	0.844	2.300	4.074
ζ Ophiuchi	1.024	3.123	1.585	0.972	2.985	2.476	0.847	2.680	1.513

Taking these model spectra as the intrinsic spectra of the target stars, we then reddened each model spectra to best match the observed spectra. Three different reddening laws were used: [Cardelli et al. \(1989\)](#) (hereafter CCM89), [Fitzpatrick et al. \(2019\)](#) (hereafter F19), and [Gordon et al. \(2023\)](#) (hereafter G23). The best fit model was determined through a two step process; first, we conducted a grid search over a large range of A_V and R_V , then using the constraints of this search we conducted a much finer grid search in a small area surrounding the suspected best fit. The models with the lowest χ^2 were taken to be the best fit models. Table 3 shows the results of these fits. Column one is the target name, column two is the best fit A_V for F19, column three is the best fit R_V for F19, column four is the associated χ^2 for F19, columns five through seven are the same for CCM89, and columns eight through ten are the same results for G23.

Because F19 and G23 are expressed as parametric fits derived from tabulated results, both F19 and G23 were implemented through the `dust_extinction` python package¹ as F19 and G23, respectively ([Gordon 2023](#)). CCM89 is implemented using the equations directly quoted from [Cardelli et al. \(1989\)](#). Because F19 and G23 were only derived for R_V s of available sight lines, neither are defined for arbitrary R_V : F19 from 2.0–6.0 and G23 from 2.3–5.6. As such, some stars in the sample exhibit R_V s that are limited by the constraints of the reddening models. For all of these cases, the best R_V reported—the lowest R_V available for the given model—was taken as the upper limit for the measured R_V for that target. Additionally, because extinction varies little in the IR at different R_V s, higher R_V gives correspondingly lower total extinction across the UV range and approximately the same extinction across the optical. As such, it requires more dust of a higher R_V to match the observed extinction in the UV range. These upper R_V values were thus taken also as upper A_V values, as an equal amount of low R_V dust produces more overall extinction than an equivalent amount of high R_V dust.

¹ <https://dust-extinction.readthedocs.io/en/stable/index.html>

Figure 7 shows the best fit extinguished model spectra for each target star, including ζ Oph, using the F19 reddening law. As before, the x-axis is wavelength in μm and the y-axis is flux in $\text{erg s}^{-1} \text{cm}^{-2} \text{\AA}^{-2}$. The blue curve represents the combined binned UV spectra and archival photometric data. The red curve shows the best fit model spectra to the data. The stellar parameters used to derive the intrinsic PHOENIX model are displayed in each figure, as well as the best fit A_V and R_V . The bottom panel shows the goodness-of-fit as represented as the residuals of the fit in terms of σ . For each of the target stars, F19 retrieves an $R_V < 2.4$, indicating extreme dust around all of the targets. ζ Oph shows normal, Milky Way average, R_V .

By plotting the data in Table 3 as a function of distance for each star, we are able to glean information on the three-dimensional makeup of the dust cloud. Figure 8 shows both the measured A_V as a function of distance and the measured R_V as a function of distance. No errors are shown for A_V or R_V . Each star is plotted at the distance derived from Gaia DR3 and is plotted in a separate color with each star labeled. Each of the three reddening laws are plotted as a different marker. Both F19 and G23 have the upper limits plotted for any derived R_V s outside of their respective defined ranges. For stars 13, 26, and 27, there is great agreement between the different models. For 4 and 24, while the reddening parameters are not consistent, the upper limits indicate rough agreement between the models. For all of the stars lying behind ζ Oph, there is a sharp drop in R_V , indicating some physical change in the dust immediately backing ζ Oph. However, all of the six targets have roughly the same A_V regardless of the distance or R_V . We interpret this as a foreground cloud of approximately Milky Way average R_V dust that does the majority of the extinction immediately preceded by a very diffuse and extremely low R_V cloud. This diffuse cloud, while not contributing much to the total extinction, contributes most of the extinction in the UV due to the extremely low R_V s, allowing for very little dust to strongly influence the measured R_V s along a sight line. As such, with the inclusion of long wavelength photometry, this study is sensitive to both R_V and A_V .

4. DISCUSSION

4.1. *Other Low- R_V Sightlines*

The presented sight line towards ζ Ophiuchi is only one of a handful of known extremely low R_V sight lines (see Gordon et al. 2003; Cardelli et al. 1989; Larson & Whittet 2005; Savage & Mathis 1979; Fitzpatrick & Massa 1988; Bohlin et al. 1978; Larson et al. 2000; Clayton et al. 2003). A selection of other reported low R_V stars is given in Table 4, which lists the stellar name along with the reported R_V and the reference for each value. Of this selection, many of the stars are bright B and A-type stars with large UV fluxes. While this could be due to the radiative influence of the hot stars on the surrounding dust, selection effects where only hot stars are classified due to their high UV flux cannot be directly ruled out.

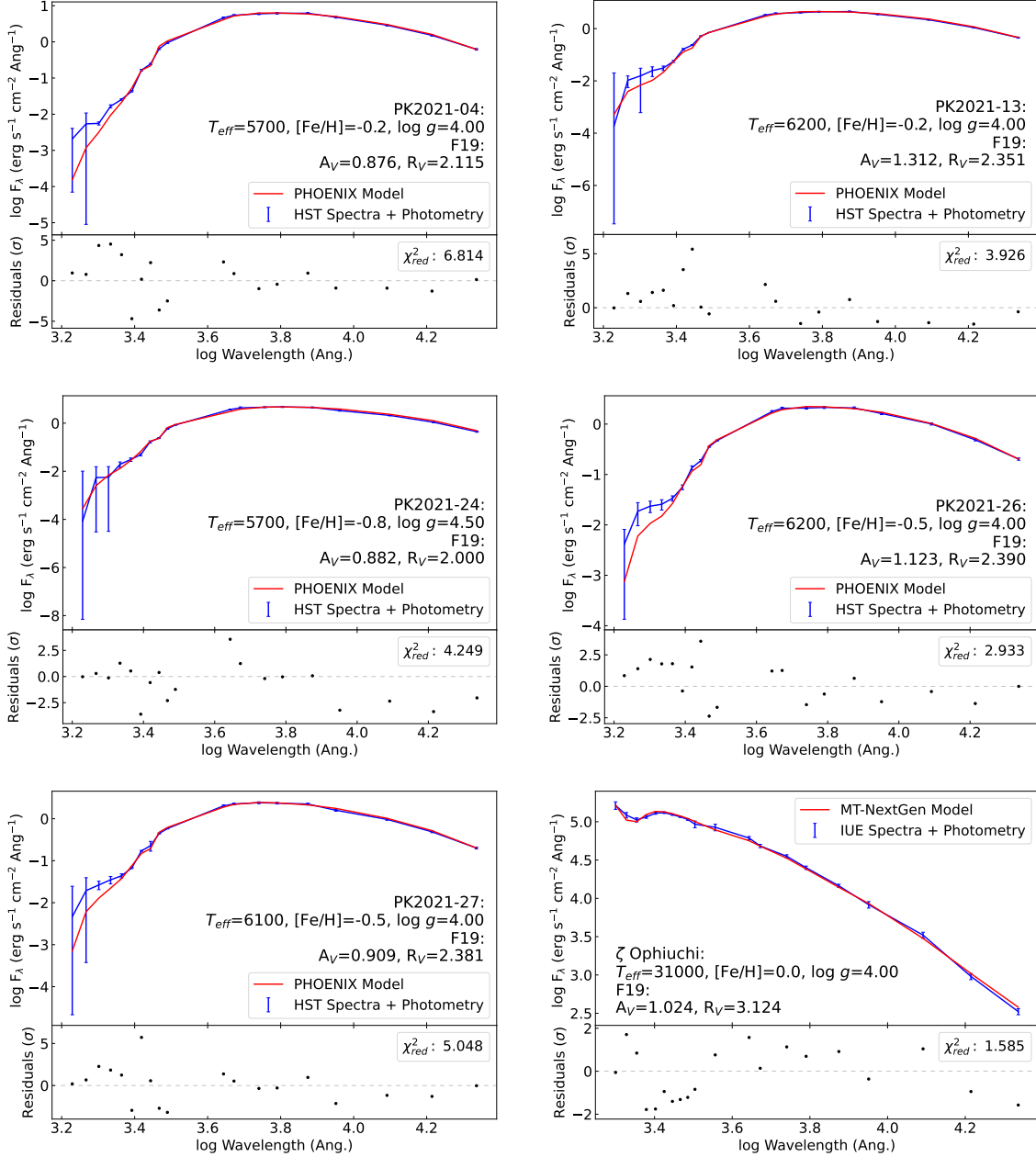


Figure 7. *Top:* The best fit extinguished model spectrum (red) plotted against the measured binned UV spectra and archival photometric data (blue). *Bottom:* The residuals of the fit in terms of number of σ away from the measured values. The corresponding χ^2 is given in the upper right. All models show relatively good fits to the data, with a largest individual data point deviation of around 5σ .

In comparison to the sight lines presented in Table 4, the sightlines toward ζ Oph have several characteristics in common: high galactic latitude, hot star, and extremely low R_V . However, very few of these sight lines have precise three dimensional reddening measurements across the field, granting us a greater insight into dust formation with the newly presented ζ Oph sightline.

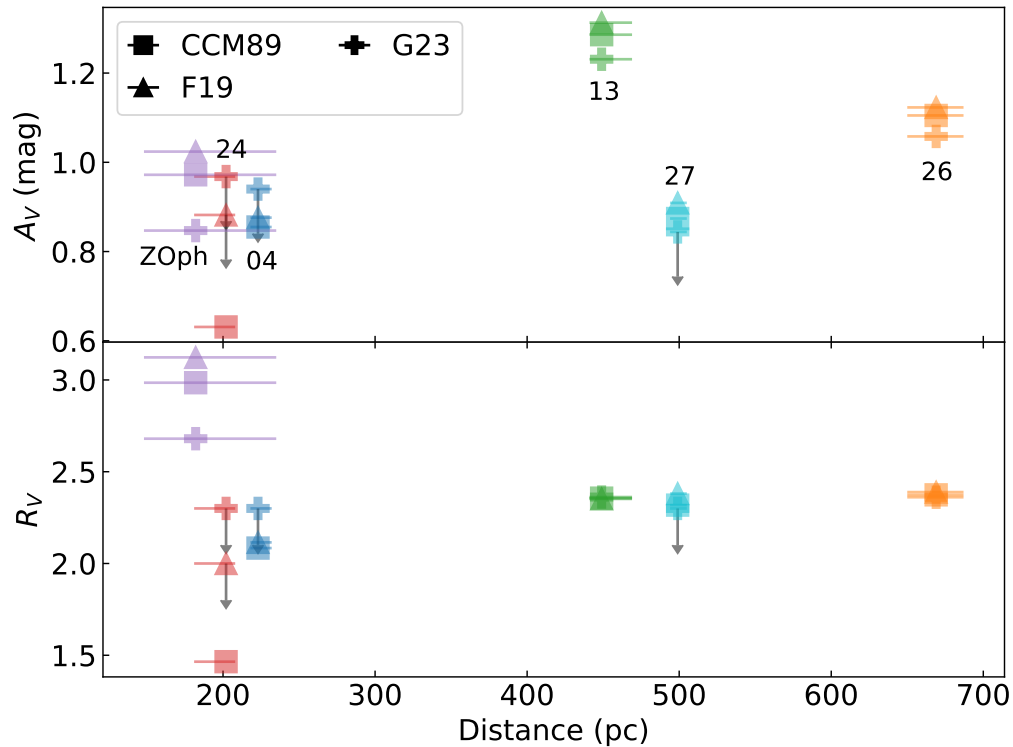


Figure 8. *Top:* Total extinction, A_V , versus distance for each star in the study. *Bottom:* Reddening law slope, R_V , versus distance for the same stars. ζ Ophiuchi shows normal Milky Way dust, whereas the target stars have extreme dust with very low R_V .

Larson & Whittet (2005) investigated the correlation of galactic latitude with measured R_V and found a correlation between low R_V sight lines and high galactic latitudes, however the reported uncertainties are very large. There thus may be a preponderance of small dust outside of the disk of the galaxy, creating systematically low R_V s for these targets. If this is the case, then the systematically smaller dust around ζ Ophiuchi may be a result of galactic formation rather than solely dust grain evolution from UV radiation. Regardless, the radiation from ζ Oph very likely has an effect on the surrounding dust grains, possibly in the form of polarization and alignment (see Piccone & Kobulnicky 2022).

4.2. Dust Grain Size Evolution

Radiation, especially from very high energy photons, can have non-negligible effects on the composition and size of dust grains. If the photons striking the dust grain have enough energy, they can begin to ionize parts of the dust grain. If this net positive charge on the grain is large enough, the mechanical strength of the grain is no longer able to hold the grain together, leading in a ‘Coulomb explosion’, blasting the dust grains apart (Draine 2011). However, if the energy is not large enough to completely tear apart the dust grain, individual ions on the dust grain can be broken off, carrying away some of the mass and charge of the grain in a process known as

Table 4. Reported Low- R_V Sightlines

Target	R_V	References
HD 210121	2.1 ± 0.2	Larson et al. (2000)
HD 204827	2.6	Bohlin et al. (1978)
HD 8153	2.14 ± 0.55	Larson & Whittet (2005)
SAO 130278	2.23 ± 0.56	Larson & Whittet (2005)
HD 24003	2.02 ± 0.95	Larson & Whittet (2005)
HD 25863	2.14 ± 0.36	Larson & Whittet (2005)
SAO 170502	2.08 ± 0.48	Larson & Whittet (2005)
HD 26434	2.27 ± 0.47	Larson & Whittet (2005)
HD 94473	2.27 ± 0.90	Larson & Whittet (2005)
HD 96237	1.44 ± 0.46	Larson & Whittet (2005)
HD 106631	2.16 ± 0.26	Larson & Whittet (2005)
HD 125679	1.91 ± 0.70	Larson & Whittet (2005)
HD 140536	2.17 ± 0.89	Larson & Whittet (2005)
HD 216308	2.21 ± 0.53	Larson & Whittet (2005)

‘ion field emission’ (Draine 2011). Overall, these two process encapsulate the idea of photoerosion due to high UV flux.

Another method for shrinking dust grains comes from high energy ions themselves rather than photons. If ions or with enough energy strike a dust grain, they can erode single atoms of the dust grain through ‘sputtering’ (Draine 2011). Because of the large UV flux around these stars, it is expected to find many ionized particles around these stars, particles that may be accelerated by the highly energetic UV photons. As the overall sizes of the particles decrease, the corresponding electron and photon cross sections become smaller, decreasing the probability of collisions, causing the size distribution to asymptotically approach a limit rather than continually shrink.

However, the probability of tearing apart a grain and the timescale to completely erode grains are such that it is very unlikely that large dust grains will erode, whereas small dust grains will erode fast. We thus expect to see sight lines around hot O-type stars of both small and large R_V , corresponding to small and large dust grains. Maíz Apellániz, J. & Barbá, R. H. (2018) finds exactly this, citing both extremely low R_V and extremely high R_V surrounding O-type stars. It is clear that more work must be done to properly understand the influence hot stars have on interstellar dust.

5. CONCLUSION

We presented new UV and optical reddening curves and the associated parameters for five target stars surrounding the hot O-type star ζ Ophiuchi. We find that the extinction curves are best characterized by extreme low $R_V < 2.4$ for the target stars and average $R_V \approx 3.0$ dust for ζ Ophiuchi. We hypothesize two different dust clouds: a thick foreground cloud with Milky Way average dust grains that provides

the majority of the extinction, and a diffuse secondary cloud with extremely small particles that produce the majority of the UV extinction. We speculate the source of the small dust grains originates from the highly UV irradiation from ζ Oph.

This sight line provides an excellent testing ground to investigate the radiative influence of hot stars on the interstellar medium. However, in order to more precisely constrain the evolution of dust grains around hot stars, more follow up work is required.

This research was made possible through the use of the AAVSO Photometric All-Sky Survey (APASS), funded by the Robert Martin Ayers Sciences Fund and NSF AST-1412587.

Facilities: *HST* (STIS)

Software: Astropy ([Astropy Collaboration et al. 2013, 2018, 2022](#)); `dust_extinction` ([Gordon 2023](#))

APPENDIX

A. UV SPECTRA

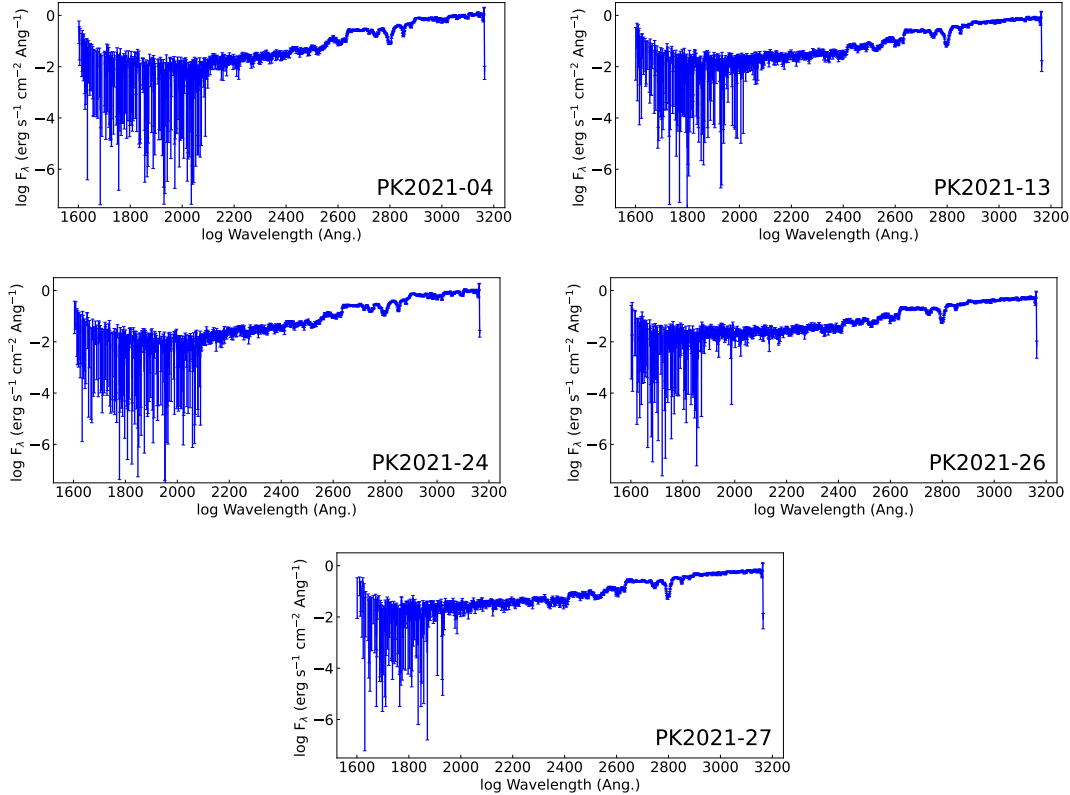


Figure 9. Raw *Hubble Space Telescope* Space Telescope Imaging Spectrograph spectra for the five target stars. All stars have very limited far-UV flux, $\lambda < 2100 \text{ \AA}$, for which the data is very noisy. Near-UV data, $\lambda > 2100 \text{ \AA}$, provide better constraints for the extinction of the star.

REFERENCES

- Astropy Collaboration, Robitaille, T. P., Tollerud, E. J., et al. 2013, *A&A*, 558, A33, doi: [10.1051/0004-6361/201322068](https://doi.org/10.1051/0004-6361/201322068)
- Astropy Collaboration, Price-Whelan, A. M., Sipőcz, B. M., et al. 2018, *AJ*, 156, 123, doi: [10.3847/1538-3881/aabc4f](https://doi.org/10.3847/1538-3881/aabc4f)
- Astropy Collaboration, Price-Whelan, A. M., Lim, P. L., et al. 2022, *apj*, 935, 167, doi: [10.3847/1538-4357/ac7c74](https://doi.org/10.3847/1538-4357/ac7c74)
- Barnard, E. E. 1910, *ApJ*, 31, 8, doi: [10.1086/141719](https://doi.org/10.1086/141719)
- Bohlin, R. C., Hubeny, I., & Rauch, T. 2020, *AJ*, 160, 21, doi: [10.3847/1538-3881/ab94b4](https://doi.org/10.3847/1538-3881/ab94b4)
- Bohlin, R. C., Savage, B. D., & Drake, J. F. 1978, *ApJ*, 224, 132, doi: [10.1086/156357](https://doi.org/10.1086/156357)
- Cardelli, J. A., Clayton, G. C., & Mathis, J. S. 1989, *ApJ*, 345, 245, doi: [10.1086/167900](https://doi.org/10.1086/167900)
- Clayton, G. C., Wolff, M. J., Sofia, U. J., Gordon, K. D., & Misselt, K. A. 2003, *ApJ*, 588, 871, doi: [10.1086/374316](https://doi.org/10.1086/374316)

- Draine, B. T. 2011, *Physics of the Interstellar and Intergalactic Medium*
- Duchêne, G., & Kraus, A. 2013, *ARA&A*, 51, 269, doi: [10.1146/annurev-astro-081710-102602](https://doi.org/10.1146/annurev-astro-081710-102602)
- Fitzpatrick, E. L., & Massa, D. 1988, *ApJ*, 328, 734, doi: [10.1086/166332](https://doi.org/10.1086/166332)
- Fitzpatrick, E. L., Massa, D., Gordon, K. D., Bohlin, R., & Clayton, G. C. 2019, *ApJ*, 886, 108, doi: [10.3847/1538-4357/ab4c3a](https://doi.org/10.3847/1538-4357/ab4c3a)
- Gordon, K. 2023, karllark/dust_extinction: OneRelationForAllWaves, v1.2, Zenodo, doi: [10.5281/zenodo.7799360](https://doi.org/10.5281/zenodo.7799360)
- Gordon, K. D., Clayton, G. C., Declair, M., et al. 2023, arXiv e-prints, arXiv:2304.01991, doi: [10.48550/arXiv.2304.01991](https://doi.org/10.48550/arXiv.2304.01991)
- Gordon, K. D., Clayton, G. C., Misselt, K. A., Landolt, A. U., & Wolff, M. J. 2003, *ApJ*, 594, 279, doi: [10.1086/376774](https://doi.org/10.1086/376774)
- Henden, A. A., Templeton, M., Terrell, D., et al. 2016, *VizieR Online Data Catalog*, II/336
- Husser, T. O., Wende-von Berg, S., Dreizler, S., et al. 2013, *A&A*, 553, A6, doi: [10.1051/0004-6361/201219058](https://doi.org/10.1051/0004-6361/201219058)
- Johnson, H. L. 1965, *ApJ*, 141, 923, doi: [10.1086/148186](https://doi.org/10.1086/148186)
- Kim, S.-H., & Martin, P. G. 1996, *ApJ*, 462, 296, doi: [10.1086/177151](https://doi.org/10.1086/177151)
- Larson, K. A., & Whittet, D. C. B. 2005, *ApJ*, 623, 897, doi: [10.1086/428877](https://doi.org/10.1086/428877)
- Larson, K. A., Wolff, M. J., Roberge, W. G., Whittet, D. C. B., & He, L. 2000, *ApJ*, 532, 1021, doi: [10.1086/308619](https://doi.org/10.1086/308619)
- Lindgren, L., Hernández, J., Bombrun, A., et al. 2018, *A&A*, 616, A2, doi: [10.1051/0004-6361/201832727](https://doi.org/10.1051/0004-6361/201832727)
- Maíz Apellániz, J., & Barbá, R. H. 2018, *A&A*, 613, A9, doi: [10.1051/0004-6361/201732050](https://doi.org/10.1051/0004-6361/201732050)
- Mathis, J. S., Rumpl, W., & Nordsieck, K. H. 1977, *ApJ*, 217, 425, doi: [10.1086/155591](https://doi.org/10.1086/155591)
- Mie, G. 1908, *Annalen der Physik*, 330, 377, doi: [10.1002/andp.19083300302](https://doi.org/10.1002/andp.19083300302)
- Morton, D. C. 1975, *ApJ*, 197, 85, doi: [10.1086/153490](https://doi.org/10.1086/153490)
- Piccone, A. N., & Kobulnicky, H. A. 2022, *ApJ*, 924, 138, doi: [10.3847/1538-4357/ac36d8](https://doi.org/10.3847/1538-4357/ac36d8)
- Savage, B. D., & Mathis, J. S. 1979, *ARA&A*, 17, 73, doi: [10.1146/annurev.aa.17.090179.000445](https://doi.org/10.1146/annurev.aa.17.090179.000445)
- Stecher, T. P., & Donn, B. 1965, *ApJ*, 142, 1681, doi: [10.1086/148461](https://doi.org/10.1086/148461)
- Trumpler, R. J. 1930, *PASP*, 42, 214, doi: [10.1086/124039](https://doi.org/10.1086/124039)
- Weingartner, J. C., & Draine, B. T. 2001, *ApJ*, 548, 296, doi: [10.1086/318651](https://doi.org/10.1086/318651)